CIRP Journal of Manufacturing Science and Technology 41 (2023) 124–134

Contents lists available at ScienceDirect

CIRP Journal of Manufacturing Science and Technology

journal homepage: www.elsevier.com/locate/cirpj

Full-length article

On the probabilistic prediction for extreme geometrical defects induced by laser-based powder bed fusion

Panayiotis Kousoulas [a,b], Y.B. Guo [a,b,*]

[a] Department of Mechanical and Aerospace Engineering, Rutgers University-New Brunswick, Piscataway, NJ 08854, USA
[b] New Jersey Advanced Manufacturing Institute, Rutgers University-New Brunswick, Piscataway, NJ 08854, USA

ARTICLE INFO

Available online xxxx

Keywords:
Powder bed fusion
Geometrical defects
Statistics of extremes
Cumulative distribution functions

ABSTRACT

Compared to traditional subtractive manufacturing processes, powder bed fusion (PBF) shows promise for making complex metal parts with design freedom, short development time, and environmental sustainability. However, there is a consensus within the additive manufacturing (AM) community that the random geometrical defects (e.g., porosity, lack-of-fusion) produced in PBF processes pose a great challenge to fabricating load-bearing parts, particularly under dynamic loading conditions. Therefore, it is imperative to quantify defect sizes and distributions to predict the critical, life-limiting defect size that significantly reduces fatigue life. This paper presents a comprehensive analysis of the defects induced by selective laser melting to quantify their sizes and statistical distributions. Then four cumulative distribution functions (i.e., Weibull, Gamma, Gumbel, and Lognormal CDFs) are leveraged and compared to predict the maximum defect size based on the principle of statistics of extremes. Both the peak over threshold (POT) approach and the block maxima (BM) approach are used for these predictions. The results show that the BM approach-based predictions for all CDFs to be much larger than the measured maxima while the POT approach-based predictions have less deviation. The Weibull and Gamma CDFs were best correlated to the data, measured by Pearson's *R* correlation coefficient, while the Gumbel and Lognormal CDFs were also well correlated.

Introduction

The quality of a printed part by powder bed fusion (PBF) process can be characterized by the geometrical defects [1], microstructures [2], and residual stress [3]. There is a consensus within the additive manufacturing (AM) community that among the concerned quality factors the random geometrical defects (e.g., porosity, lack-of-fusion) pose the greatest challenge to fabricating load-bearing parts, particularly fatigue performance in dynamic loading conditions. Technically, a defect renders a part defective. Some geometrical inhomogeneities are tolerable due to their relatively small size due to their relatively small size and low volume fraction. Thus, as Snow et al. note [4] the term 'flaw' is more appropriate as a general label for pores and cracks. Since this paper focuses on critical flaws, the term 'defect' will be used. The geometrical defects can be mainly measured optically or with X-ray computed tomography (CT) [5], and both approaches have been applied to studies of PBF parts (e.g., [6]). Excluding surface roughness, the main geometrical defects are porosity (e.g., gas pores) and lack-of-fusion (LOF, e.g., un-melted particles). Porosity is often caused by insufficient energy input, while the LOF defects result from excess energy input. It is desirable to control these defects by optimizing process parameters, as has been studied extensively (e.g., [7]). Finding a suitable method of predicting the geometrical defects of geometrical defects for certifying the AM parts is of great interest [1,8–12].

The effect of the geometrical defects on the fatigue performance of PBF parts is a prominent area of research [1,3,10,13–15]. The fatigue characteristics of AM materials must be understood and controlled to meet design requirements. For example, the high surface roughness from unmelted particles on the part surface lowers the fatigue life and fatigue strength in bending [15]. Tension-compression fatigue testing has shown that the geometrical defects are just as harmful as surface roughness [16]. It has been shown that post-processing surface finishing (e.g., [17], [18]) and hot isostatic pressing (HIP) [1] can increase the fatigue strength of L-PBF parts by eliminating or reducing the size of internal defects and relieving residual stresses.

Fatigue data of PBF specimens are distinctly unpredictable, i.e., scattering, due to the random geometrical defects. The scattering can

* Corresponding author at: Department of Mechanical and Aerospace Engineering, Rutgers University-New Brunswick, Piscataway, NJ 08854, USA.
E-mail address: yuebin.guo@rutgers.edu (Y.B. Guo).

https://doi.org/10.1016/j.cirpj.2022.11.024
1755-5817/

be organized into three different observed cases: identical prints giving different fatigue lives [19,20], different lives for as-built vs. post-processed samples [21–23], and different lives for different materials made under the same process conditions [24]. Identical printings using same process parameters may generate different life-limiting defects due to uncertainties in the melting and solidification process. Post-processing can relieve residual stresses, modify surface roughness, and mitigate internal defects of as-printed materials, therefore, improve fatigue performance. Furthermore, different materials will have different properties even under same processing conditions, which causes different lives.

Quantifying the determinantal effect of geometrical defects on fatigue limit and its scattering is contingent on the termination of the defect sizes and distributions. The literature uses the estimation method proposed by Murakami to predict the maximum effective size $\sqrt{area}_{\max}$ of irregularly shaped defects [15], where the $\sqrt{area}_{\max}$ parameter is defined as the square root of the defect area normal to the direction of maximum tensile loading. This method is based on the Gumbel cumulative distribution function (CDF). On the other hand, there are three alternative CDFs, i.e., Weibull, Gamma, and Lognormal CDFs. However, which CDF may give the most accurate prediction of the maximum effective size has yet to be investigated. This question leads to the following objectives of this study:

- Assess the state-of-the-art predictive methods of geometrical defects in metal AM
- Conduct a comprehensive characterization of a wide range of geometrical defects produced in laser-based PBF (L-PBF)
- Benchmark the performance of the Weibull, Gamma, and Lognormal CDFs vs. the Gumbel CDF by comparing with the predicted maximum effective defect sizes vs. the measured data

State-of-the-art analysis

Geometrical defects formation mechanisms

PBF-induced geometrical defects can be grouped based on their mechanisms of formation. As summarized by Snow et al. [4] these defects are gas porosities, melt pool instabilities, and regions with a lack of fusion (LOF). (1) Gas pores are identified as near spherical voids within a printed part, and typically are the smallest in size of all three defect groups. These are introduced into the solidified metal either by the release of trapped gas inside the virgin (i.e., unmelted) powder stock or by gas bubbles enveloped by the melt pool. (2) Melt pool instabilities result in voids and pores due to the vaporization loss. At higher energy inputs, more molten metal from the melt pool can evaporate. This occurs when high energy densities are applied when using high laser powers and slow scanning speeds or when deceleration of the laser exposes the area of the powder bed incident to the energy source for more time. (3) LOF can occur systematically and stochastically, generally resulting in large, irregular voids, often identified by partially melted powder inside voids. Laser power and scanning speed parameters must be optimized to ensure subsequent scanning passes completely fuse both and with any previously solidified material below. Even with optimized parameters, random LOF defects may still occur due to the highly volatile PBF process. The unmelted powder can contaminate the melt pool as a spatter or powder is blown by inert shielding gas and cause incomplete fusion.

Geometrical defect morphology characterization

Morphology (morph- from the Greek μορφή, or form) is a key part of characterizing defect size and shape in PBF. As discussed in the preceding section, based on the shape and size of a defect the formation mechanism responsible for its creation can be identified. Thus, by characterizing defect geometry and location within a component, manufacturers can determine the root causes of any defect formation and tune their process parameters accordingly.

Morphology studies of internal defects originally required destructive methods (e.g., mechanical cutting) to investigate samples. By taking slices or sections of a sample, a 2D inspection area of the interior geometry can be observed by optical methods (e.g., [16]). While this method is simple and easy for most investigators to perform, the nature of the destructive method of inspection does not leave the part intact for additional testing. This is not altogether unfavorable if simultaneous studies can be performed on the same sliced sample, e.g., microstructure formation and hardness. Yet, it still restricts morphology analysis to 2D descriptions of defect size and shape.

X-ray computed tomography (CT) is a popular non-destructive method of detecting internal cracks and porosity and measuring defect sizes [9,25–31]. While being expensive and time-consuming, CT can resolve the entire population of internal defects in each sample region and accurately portray not only 2D but also the 3D shape of defects with additional image processing. This allows direct 3D quantification of defects (e.g., population, volume fraction, sphericity, spatial orientation). Of course, the limiting size of defects that can be detected depends on the maximum resolution available, which can be on the order of tens of microns [32].

Juan et al. [33] presented a hybrid destructive and non-destructive investigative method for characterizing metal inclusions, first using scanning ultrasonic microscopy to detect the location of large internal defects and then dissecting the specimen to better observe the defects with scanning electron microscopy. While this does help to reduce the risk of missing or overlooking critical defects in a part, it lacks the advantage of 3D defect characterization.

3D representations of defects can be used to quantify the regularity or irregularity of defect shape. The measure of sphericity is the ratio of sphere surface area to defect surface area for a sphere with equal volume to the defect. Sphericity close to one will result in near-spherical defects while low sphericity values denote irregular defects.

Equivalent diameter is a measure of 3D defect size, defined as the diameter of a sphere of equal volume [33]. This may not be suitable for elongated, irregular pores (e.g., LOF) since such defects may misrepresent how detrimental long, crack-like defects with relatively small areas can be to the fatigue performance of PBF components [34].

For 2D observations of defects, the maximum effective size $\sqrt{area}_{\max}$ parameter adopted in Murakami's work [35,36] is a popular choice for representing defect size [8,9,26,28,31,37], partly because it is used to predict the fatigue limit of PBF components. This gives a 1D (length) measurement to represent the 2D (area) size of the defect. In some cases, defects are grouped closely together, making it difficult to assume the individual defects to be independent of or unaffected by the group. There are also times when defects are close enough to the part surface that the area between the defect and the surface does not offer much structural integrity. In these situations, an effective defect size [1] can be taken to estimate the total area affected by the sub-surface or interacting defects by drawing around the outer borders of the affected region to completely envelop all defects and/or the sub-surface defect area and the area immediately separating it from the free surface. Naturally, this requires the use of image analysis software, which is often included in optical measurement systems.

These methods are not intended to precisely measure actual defect size but rather estimate an effective crack length with approximately the same impact. This was explained by Murakami and Endo through their investigation by comparing artificial defect holes with specific diameters to non-propagating cracks in steel specimens [38]. The level of precision of the measured area depends on how closely drawn the enveloping contour is to the actual

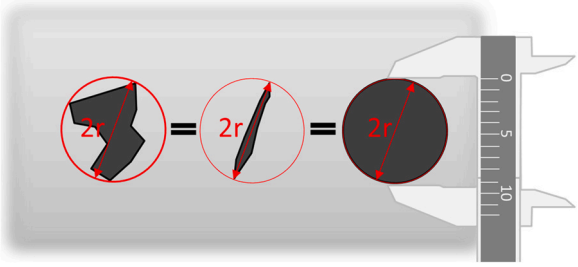

Fig. 1. Schematic of Feret caliper (FC) diameter.

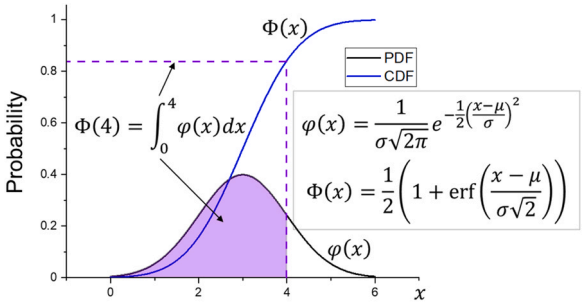

Fig. 2. Schematic of the normal distribution (PDF φ and CDF Φ).

boundaries of the defect. As mentioned by Oberreiter et al., higher precision can be more favorable for accurately depicting the actual defect area, which comes at the price of more complicated and tedious creation of the contours in image analysis software [31].

Possibly more accurate measurement of defect size is the maximum Feret or Feret caliper (FC) diameter [39]. The FC diameter measures the distance between two points across from each other on the boundary of interest, and was used by Nicoletto et al. [40] in measuring the size of metallographically observed casting defects. The distribution of defect sizes was used in comparison to the $\sqrt{area}_{max}$ parameter in Murakami's work to predict the maximum defect size, resulting in much larger predictions, yet well correlated, nonetheless. The predicted critical defect sizes using the FC diameter description also yielded closer approximations of fatigue strength of cast AlSi7Mg.

The FC diameter is also advantageous over area measurements because it carries physical significance whereas area measurements are more abstract in concept. To illustrate this point, consider an irregular pore inscribed inside a circle of radius r (see Fig. 1). The longest dimension of the pore should be approximately equal to the circle diameter $2r$. In most cases, the inscribed pore will not cover all the area of the circle circumscribing it. Even for a perfectly circular pore, its area would be πr^2, which would result in a 1D defect size of about $1.772r$ using the $\sqrt{area}$ parameter method.

Extreme of statistics-based prediction method for defect size

The aim of the statistical theory of extreme values, in application to porosity, is to analyze observed pores in a printed sample and to forecast further extremes [41] (e.g., a maximum pore size). Extremes are rare events that are not often observed. The lower and upper bounds can be estimated probabilistically by extrapolating from the available data. This relies on certain functions, namely the probability density function (PDF) and the cumulative distribution function (CDF). The PDF describes the relative frequency of a continuous distribution of values and is analogous to a histogram of discrete data. The CDF describes the cumulative frequency of a continuous distribution of values. By definition, the CDF is the integral of the PDF. Fig. 2 gives an example plot of the well-known normal distribution, which has a PDF shaped like a bell.

In application to predicting the extreme defect sizes, the values at the left and right tails of a PDF are of interest. These regions correspond to the extreme minima and maxima of distribution, respectively. While a CDF can output the probability for a given range of values, the inverse of the CDF can be used to solve for the values, given a probability. In this way, a prediction can be made about extreme values corresponding to a set probability.

Table 1 lists different CDFs used in the literature to predict extreme sizes of defects in metals. Generalized distributions, like the Generalized Extreme Value (GEV) and Generalized Pareto (GP), are good starting points for modeling defect data but simultaneously more tedious to apply since they represent the most general case with no simplifying assumptions. Anderson et al. [37] compared the precision of estimates of the maximum inclusion size in a steel bar made using GEV and GP distributions of inclusion data as well as simplified forms of the two distributions. Their results showed higher precision with the GP estimate in comparison to the GEV estimate and further showed an increase in precision for the simplified distributions. The simplification of the GEV and GP distributions was setting the shape parameter to zero. This changed the GEV distribution to a Gumbel distribution (Eq. (1)) and the GP distribution to an Exponential distribution (Eq. (2)). Overall, the Exponential distribution gave the narrowest confidence intervals.

$$F(x) = \exp\left[-\exp\left(\frac{x-\mu}{\sigma}\right)\right] \tag{1}$$

$$F(x) = 1 - e^{-\lambda x} \tag{2}$$

While the same inclusion data (measuring $\sqrt{area}_{max}$ larger than a threshold of 5 µm) was used for all the predictions, the GEV and Gumbel distributions used only the maximum inclusion sizes measured from each inspection area (called the block maxima (BM) approach [32]) while the GP and Exponential distributions used all inclusion sizes above the threshold (called peak over threshold (POT) approach [32]). Murakami followed the block maxima approach in his earlier publications on metallic inclusions in steel (e.g., [16]). By

Table 1
Representative cumulative distribution functions (CDFs) for defect analysis.

Distribution (s)	Application	Reference
GEV, GP	Predicting maximum inclusion size in steel	[37]
Lognormal, Gumbel	Predicting maximum inclusion size in steel	[33]
Gumbel	Predict maximum defect size in SLM-ed Ti6Al4V	[28]
GEV	Predicting maximum inclusion size in steel	[8]
Gumbel	Size distribution of pores in L-PBF-ed SS-316L	[30]
GEV	Evaluation of probability of occurrence of fracture-initiating defects	[31]
GP, Gumbel	Estimate maximum defect from CT data	[32]

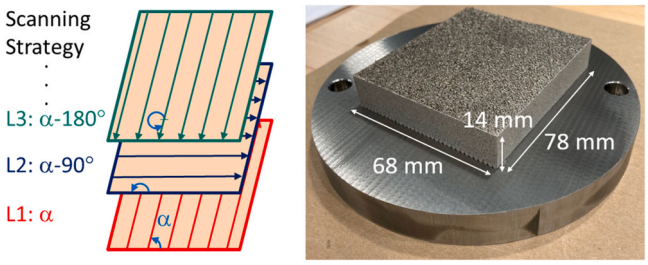

Fig. 3. SLM scanning strategy and printed SS-316L block.

observing a set area of steel from different sample slices, only the maximum inclusion from each observed area would be recorded. In this way, only a distribution of the maximum inclusions relative to the set inspection area would be modeled, as detailed by Gumbel regarding the statistics of extremes [41].

Juan et al. [33] showed the distribution of metallic inclusion size (equivalent diameter) to follow a lognormal distribution. However, a definition of inclusion size was not explicitly given. It is inferred from the study that the longest dimension of an observed inclusion cross section was taken as the defect size.

By analyzing the literature, several essential questions in probabilistic modeling remain to be investigated, i.e., how much data needs to be measured to yield a reliable prediction, which CDF best describes the defect size, and which approach (BM or POT) is appropriate for use [32,42].

Sample fabrication, preparation, and characterization of geometrical defects

SLM of SS-316L block and sample preparation

An AconityMiNi SLM printer was used to print a rectangular SS-316L block 14 × 68 × 78.08 mm^3 in a flowing argon environment. The block was printed with a 90-degree cross-hatching scanning strategy (see Fig. 3). The top face (68 × 78.08 mm^2) lay parallel to the substrate, with the vertical dimension of 14 mm oriented in the build-up direction. The process parameters (see Table 2) were selected intentionally to produce a wide range of geometrical defects throughout the block.

To expose the printed geometrical defects, wire-EDM was used to section the sample for measurement. Fourteen slices were taken from the sample block to quantify the size of the defects and their distribution through optical metrology. The sample slices were designed with a dog bone geometry to be used in future fatigue testing.

Wire-EDM is a thermal process where high discharging energy was applied between a thin wire (e.g., brass with 0.25 mm diameter in this experiment) and the metal block and erodes the material along a prescribed path. The thermal nature of wire-EDM introduced a heat-affected zone (HAZ) at the workpiece surface. The EDMed surfaces of each sample were prepared using a two-stage grinding

Table 2
SLM process parameters.

Parameter	Value	Units
Laser Power	250	W
Laser Diameter	0.050	mm
Scan Speed	800	mm/s
Layer Thickness	0.050	mm
Hatch Spacing	0.070	mm

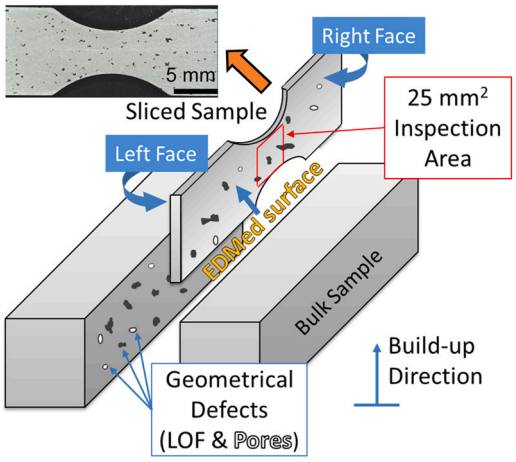

Fig. 4. Illustration of wire-EDM sampling.

followed by polishing after wire-EDM. This removed the HAZ from the samples so only the as-SLMed microstructure and related mechanical properties would be subjected to measurement. Polishing also gave a smooth surface for inspecting pores with optical microscopy. First, 220 grit sandpaper was used to remove the HAZ, then 1000 grit sandpaper was used to remove the grinding marks from the previous step and polish the surfaces to an average *Sa* 1.5 µm. During the grinding and polishing processes, cold tap water was used to eliminate frictional heat to avoid the potential of altering the as-printed microstructure and flush away loose particles. Fig. 4 shows the exposed geometric defects (i.e., pores and LOFs) on the sliced sample.

Characterization of geometrical defects

Each sample was inspected using a Keyence VR 3100 optical microscope. 3D surface topography of the right and left faces was also measured to quantify the surface roughness of the polished samples. The surface roughness of a 1 × 1 mm^2 area free of pores was inspected on the right and left faces of each sample. The number of defects and their sizes inside a 5 × 5 mm^2 measurement area of each sliced sample surface were counted and measured using the Feret caliper (FC) method (see Fig. 5).

The FC diameter pore size was quantified by inscribing each pore within the smallest circle possible and using the resulting diameter

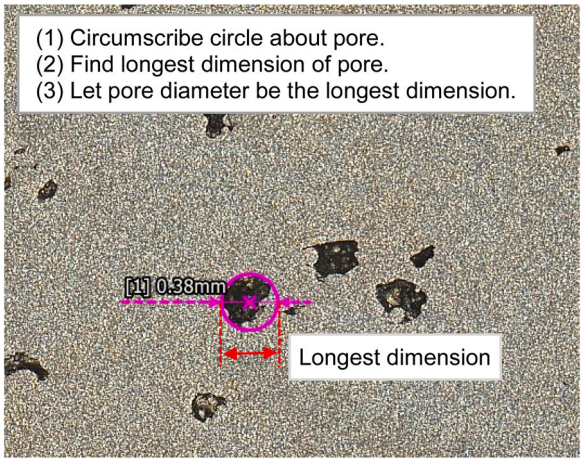

Fig. 5. Feret caliper (FC) method for measuring defect size.

Table 3
Cumulative distribution functions (CDFs).

	Gumbel	Weibull	Gamma*	Lognormal*
CDF	$F(d) = e^{-e^{\left(\frac{d-\mu}{\sigma}\right)}}$	$F(d) = 1 - e^{-\left(\frac{d}{\alpha}\right)^{\gamma}}$	$F(d) = \frac{1}{\beta^{a}\Gamma(a)}\int_0^d x^{a-1}e^{-\frac{x}{\beta}}dx$	$F(d) = \Phi\left(\frac{\ln d-\mu}{\sigma}\right)\Phi$= standard normal CDF (see Fig. 2)
Reduced Variate	$y = \frac{d-\mu}{\sigma}$	$y = \frac{d}{\alpha}$	$y = d$	$y = d$
Parameters	$\sigma = -\frac{1}{m}\mu = b\sigma$	$\alpha,\ \gamma \neq 0\alpha = \frac{1}{m}$	mean of $d = a\beta$	$\mu = \ln$(mean of $d)\sigma$ = stand. dev. of ln$d$
Inverse CDF	$y_j = -\ln[-\ln(F_j)]$	$y_j = [-\ln(1 - F_j)]^{\frac{1}{\gamma}}$	y_j = GAMMA. INV(F_j, a, β)	y_j = LOGNORM. INV(F_j, μ, σ)
Regression Equation	$y = md + bm = -\frac{1}{\sigma}b = \frac{\mu}{\sigma}$	$y = md + bm = \frac{1}{\alpha}$	$y = md + b$	$y = md + b$

*Inverse CDF given as Microsoft ® Excel ® function

as an effective defect size. The grouping or clustering effect of defects was not accounted for in the size of the defects. Only individual pores were measured to simplify this study. A total of 769 pores were collected and measured.

Prediction of extreme defect size with alternative CDFs

Dataset characteristics and distributions

To benchmark the popular Gumbel CDF for predicting the maximum defect size in metal AM, four different CDFs are listed in Table 3, as well as definitions of their parameters and regression equations.

Seven different cases were investigated to predict the maximum defect size from the collected porosity data. The first six cases follow the peak over threshold (POT) approach of using all data above a threshold value. The last case follows the block maxima (BM) approach of only using the maximum defect size measured from each inspection area.

While the BM approach limits the amount of data used to the number of inspection areas, the POT approach allows the flexibility of varying the amount of data used by setting a threshold. This can be seen as an optimization problem involving a balance between sample size and level of defect magnitude. By varying the amount and magnitude of the data used by the POT approach, the possible dependence of the predictions on these factors can be investigated. The six POT cases are as follows.

Case 1. : Entire dataset (threshold set to be below the minimum measured pore size).

Case 2. : Dataset from the right face of each sliced sample (same threshold as Case 1, just less data).

Case 3. : Dataset from every other right face of each sliced sample (see Fig. 4).

Case 4. : Dataset with defect size threshold to 100 µm (i.e., data exceeding 100 µm).

Case 5. : Dataset with defect size threshold of 212.93 µm (i.e., data equal to and above the median value of all data).

Case 6. : Dataset with defect size threshold to only keep the largest 100 defects.

For the BM approach, the largest defect size from each of the 28 inspection areas is used for linear fitting and extrapolation. Each distribution gives an estimate of the largest expected defect size, corresponding to a cumulative probability of 99.9%. The predictions are compared to the measured data and a discussion of the results is given.

Table 4 gives descriptive measures of each of the datasets used for the comparative approaches. Fig. 6 shows the histograms of the data from each of the 6 POT cases, which all have the same general trend of being right-skewed.

Procedure for predicting maximum defect size

The procedure used to predict the defect size corresponding to a certain cumulative probability (e.g., 99.9%) of not being exceeded is as follows.

(1) Sort the porosity data in ascending order and assign each value a rank j (e.g., smallest pore has rank $j = 1$, next smallest has rank $j = 2$, continue up to largest pore with rank equal to sample size n).
(2) Find the Cumulative Distribution Function (CDF) value F_j for each pore using Eq. (3).

$$F_j = \frac{j}{n+1}, \tag{3}$$

(3) Find the inverse CDF value y_j for each pore using the respective equations from Table 3 with F_j from step 2.
(4) Plot the pore diameters in ascending order against the corresponding inverse CDF values.
(5) Apply the Method of Least Squares (MLS) to fit a linear (regression) line to the data.

Table 4
Descriptive measures of porosity distributions.

POT or BM	Sample size	Mean (µm)	Median (µm)	Standard Deviation (µm)	Minimum (µm)	Maximum (µm)
Case 1	769	274.025	212.933	221.029	26.236	1525.947
Case 2	383	264.801	209.587	209.593	26.236	1231.468
Case 3	178	282.195	221.573	220.991	26.236	1231.468
Case 4	612	327.017	272.667	218.041	100.099	1525.947
Case 5	385	429.978	359.801	215.199	212.933	1525.947
Case 6	100	724.563	674.920	210.848	499.315	1525.947
BM	28	899.803	898.639	244.184	423.006	1525.947

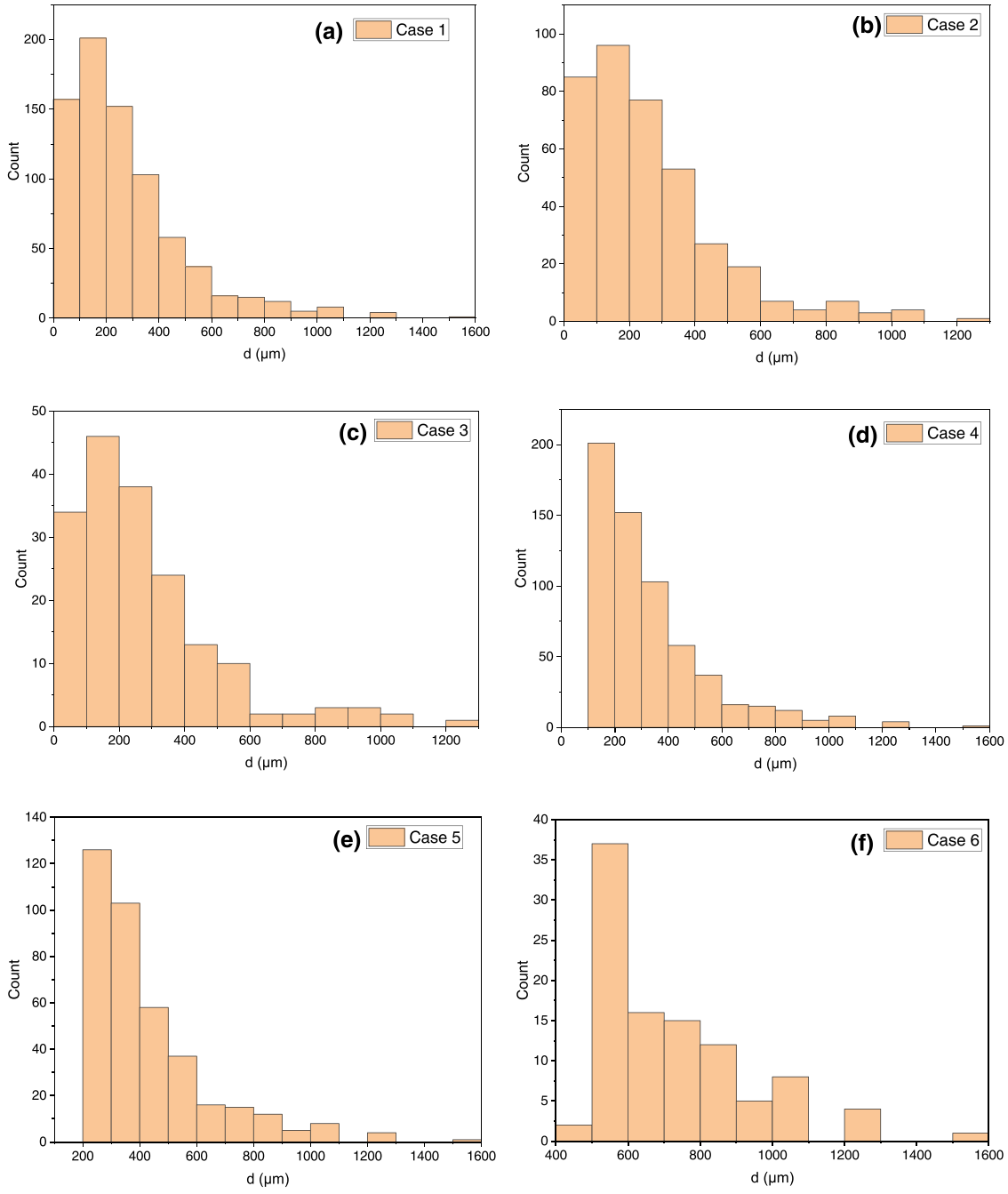

Fig. 6. Histograms of the six data cases used for the POT approach.

(6) Extrapolate from the regression equation to find the maximum defect size (at a given probability, e.g., 99.9% @ $F_j = 0.999$) (granted, of course, the regression line is well-correlated to the data).

The resulting predicted sizes are compared to the maximum diameter of each dataset to quantify how much the predictions deviate from the measurements. Pearson's R, defined as

$$\boldsymbol{R} = \frac{1}{\boldsymbol{n-1}} \frac{\sum_{\boldsymbol{j=1}}^{\boldsymbol{n}} (\boldsymbol{d_j} - \bar{\boldsymbol{d}})(\boldsymbol{y_j} - \bar{\boldsymbol{y}})}{\boldsymbol{s_d s_y}}, \quad \boldsymbol{-1 \le R \le 1}, \tag{4}$$

is used as a correlation factor to compare the goodness of fit of each CDF. $\boldsymbol{s_d}$ and $\boldsymbol{s_y}$ are the sample standard deviations of the measured pore diameter $\boldsymbol{d}$ and reduced variate/inverse CDF value $\boldsymbol{y}$, respectively, while $\bar{\boldsymbol{d}}$ and $\bar{\boldsymbol{y}}$ are their mean values. Regressions with $\boldsymbol{R}$ close to 1 signify a good correlation between $\boldsymbol{d}$ and $\boldsymbol{y}$. For CDFs with shape

Table 5
Predicted maximum defect sizes (rounded) using regression equations from Table 6.

CDF	POT Case or BM	Prediction (μm)	% Difference from case maximum
Gumbel	Case 1	1398	-8%
	Case 2	1339	9%
	Case 3	1438	17%
	Case 4	1441	-6%
	Case 5	1542	1%
	Case 6	1843	21%
	BM	2306	51%
Weibull	Case 1	1606	5%
	Case 2	1546	26%
	Case 3	1665	35%
	Case 4	1646	8%
	Case 5	1744	14%
	Case 6	1884	23%
	BM	5861	384%
Gamma	Case 1	1552	2%
	Case 2	1492	21%
	Case 3	1665	35%
	Case 4	1646	8%
	Case 5	1744	14%
	Case 6	1931	27%
	BM	2623	172%
Lognormal	Case 1	2161	42%
	Case 2	2113	72%
	Case 3	2302	87%
	Case 4	1799	18%
	Case 5	1635	7%
	Case 6	1723	13%
	BM	2168	42%

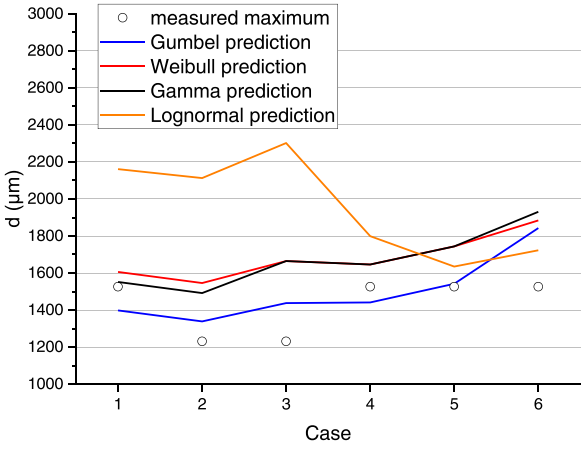

Fig. 7. POT prediction deviation from the measured ones.

parameters (i.e., the Weibull and Gamma CDFs), an initial guess is used to generate a value for ***R***. Then the shape parameter value is tuned to give an ***R*** value closest to one. The regression equation associated with the tuned shape parameter is then used in step 6 of the prediction procedure.

Table 5 lists the predictions of each CDF and their deviations from the measured maxima of each data case, which is graphically displayed in Fig. 7. POT cases 3–5 had matching predictions for the

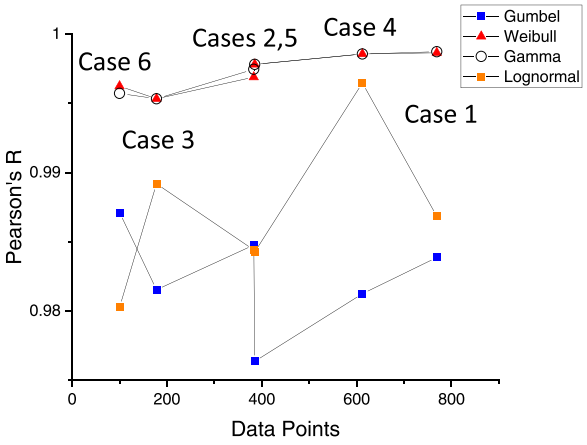

Fig. 8. POT approach goodness of fit dependence on amount of data.

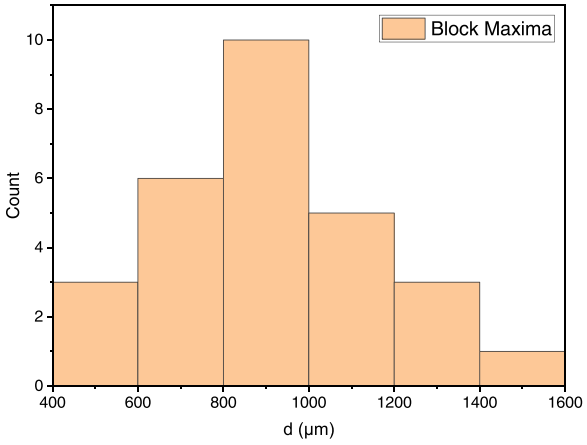

Fig. 9. Histogram of porosity data for BM approach.

Weibull and Gamma CDFs, and predictions for POT cases 1, 2, and 6 for these two distributions were also similar. Overall, the Weibull and Gamma CDFs resulted in the highest correlations (see Fig. 8) for all POT cases. Increasing the sample size may have slightly raised the *R* values for the Weibull and Gamma CDFs, while no clear trend is visible for the Gumbel and Lognormal CDFs. From a broader perspective, however, each CDF was able to correlate well to the porosity data for the POT approach, with all maximum *R* values being above 0.975. The Gumbel CDF yielded predictions below the measured maxima for POT cases 1 and 4. The Lognormal CDF had the largest prediction deviations for POT cases 1–3, where the threshold value was kept at its lowest (essentially zero). The Lognormal CDF had much more similar predictions to the other CDFs for POT cases 4–6 where the threshold value was increased successively, although the prediction deviation did not seem affected by these consecutive changes.

A histogram of the maximum pore sizes used for the BM approach is shown in Fig. 9, which is normally distributed. All the BM predictions have deviated from the measured maximum pore size of

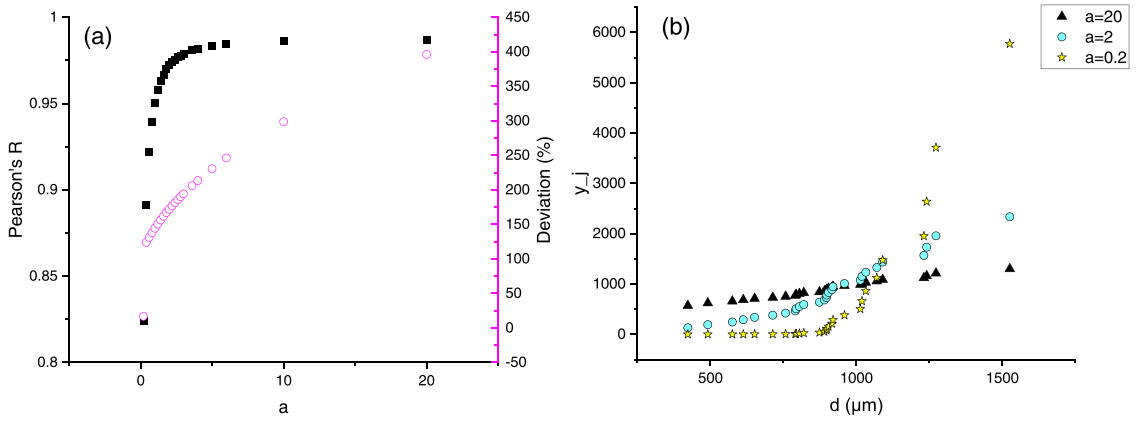

Fig. 10. Gamma CDF shape parameter tuning, BM method: (a) Shape parameter a v.s. Pearson's R and % deviation of prediction; (b) Inverse Gamma CDF plotted at shape parameters a = 0.2, 2, 20.

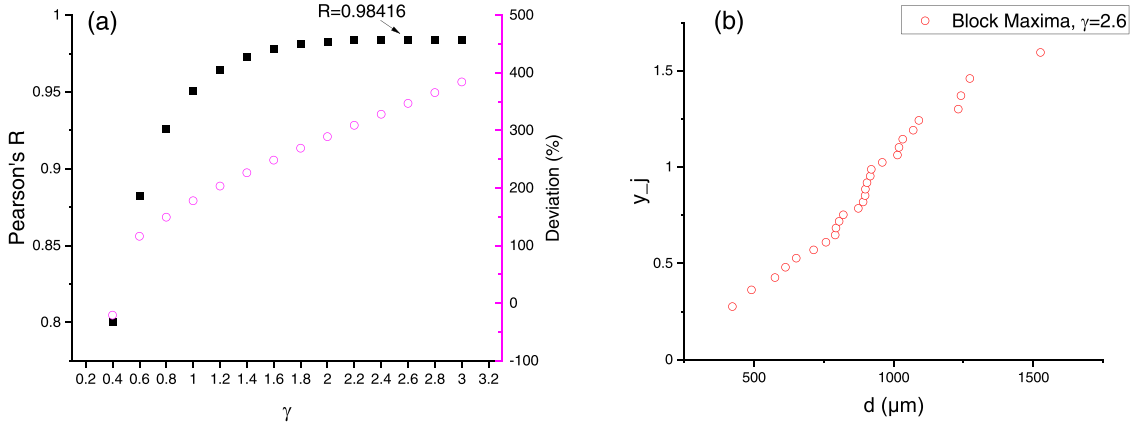

Fig. 11. Weibull shape parameter tuning, BM approach: (a) shape parameter γ v.s. Pearson's R and % deviation of prediction; (b) Inverse Weibull CDF with γ = 2.6, the case with the largest R value.

about 1526 μm, which the minimum prediction exceeded by 42% (see Table 5). In comparison, assuming from Fig. 9 that the maximum defect size is normally distributed, the empirical rule (a.k.a, the 68–95–99.7 rule) can be used to predict the maximum defect. Using the sample mean and sample standard deviation for the BM approach data from Table 4, approximately 99.85% (99.7% within three standard deviations of the mean and an additional 0.15% of smaller values outside this interval) of all observations will be less than a defect with a size three standard deviations larger than the mean, which equals about 1632 μm. This prediction has only a 7% deviation from the measured maximum and is more realizable than the BM approach-based predictions.

While the Weibull and Gamma CDFs could be tuned to correlate well to the data from the POT approach, tuning their shape parameters with the data from the BM approach gave unrealistic results. Figs. 10–11 depict the results of tuning the shape parameters to give R values closer to 1. While the CDFs were become increasingly well correlated, the prediction deviations rose dramatically. A maximum R value was reached for the Weibull distribution with γ = 2.6 while the Gamma CDF prediction deviation continued to grow when approaching an upper limit for R (see Fig. 10). Whenever extrapolation methods are used, therefore, one must be careful not to rely only on regressions that are highly correlated to the data and must ensure that the regression gives realistic results.

Table 6 shows the CDF parameter values and regression equation slope and intercept values corresponding to the highest R values, except for the Gamma CDF regression with the BM approach, where the tuning of the shape parameter showed an almost unbounded rise in the prediction deviation when approaching larger R values (see Fig. 10). It is interesting to note that the shape parameter γ = 1 for the Weibull CDF gave the best correlation for all but the 6th POT case. This simplifies the Weibull 2-parameter CDF to become the Exponential distribution, which only has one parameter.

Table 6
Linear regression results with the highest R^* (in bold).

CDF	POT Case or BM	Linear regression			Distribution parameters		
		Method of Least Squares		Correlation Coefficient	Shape	Scale	Location
		Slope m	Intercept b	Pearson's R		σ	μ
Gumbel	Case 1	0.005636	-0.97067	0.983876		-177.419	172.2157
	Case 2	0.005898	-0.99047	0.984766		-169.56	167.9441
	Case 3	0.005487	-0.98223	0.981543		-182.247	179.0092
	Case 4	0.005685	-1.28585	0.981249		-175.911	226.1962
	Case 5	0.005695	-1.87768	0.976372		-175.577	329.679
	Case 6	0.005677	-3.55318	0.987116		-176.155	625.9121
	BM	0.004531	-3.54230	0.98337986		-220.726	781.878
		m	b	R	γ	α	
Weibull	Case 1	0.004439	-0.22049	0.998651	1	225.2988	
	Case 2	0.004618	-0.23044	0.996892	1	216.5397	
	Case 3	0.004282	-0.22252	**0.995329**	1	233.5283	
	Case 4	0.004484	-0.47159	**0.998561**	1	222.9949	
	Case 5	0.004502	-0.94347	**0.997812**	1	222.1021	
	Case 6	0.003517	-1.6222	**0.99624**	1.2	284.2977	
	BM	0.001371	-0.35010	0.98415738	2.6	729.216	
		m	b	R	a	β	
Gamma	**Case 1**	1.112191	-31.7277	**0.998726**	1.2	228.3547	
	Case 2	1.119871	-33.4478	**0.997463**	1.2	220.6682	
	Case 3	1.2084	-62.7939	**0.995329**	1	282.1956	
	Case 4	1.466478	-154.218	**0.998561**	1	327.0172	
	Case 5	1.93595	-405.674	**0.997812**	1	429.9786	
	Case 6	2.545674	-1130.57	0.995721	1.6	452.852	
	BM	2.222616	-1127.6933	0.972113648	2	449.901	
		m	b	R		σ	μ
Lognormal	Case 1	1.50089	-37.6857	0.986847		0.795823	5.61322
	Case 2	1.50419	-37.6993	0.984419		0.800342	5.578982
	Case 3	1.46731	-33.0888	0.989186		0.800097	5.6426
	Case 4	1.11294	23.8003	0.99647		0.590194	5.790013
	Case 5	0.92375	71.5436	0.984271		0.421622	6.063735
	Case 6	0.90351	93.9785	0.980285		0.266377	6.585569
	BM	0.983824	44.53503	**0.985147839**		0.286	6.802

*For Gamma CDF's regression higher values of R are possible, but predictions become highly deviated from the measured maximum pore diameter.

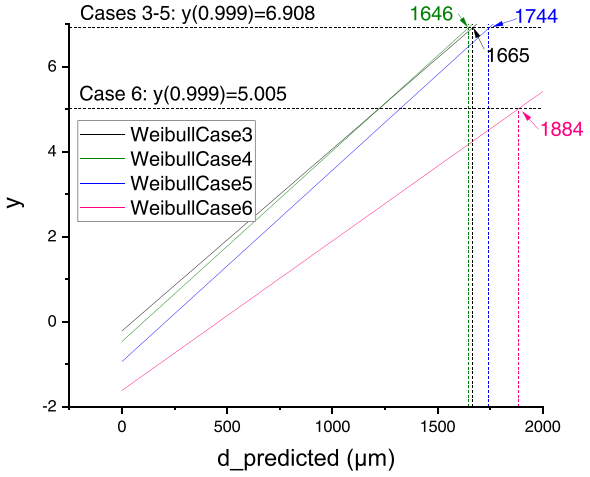

Fig. 12. Weibull regression lines for extrapolating maximum defect size, POT approach, cases 3–6.

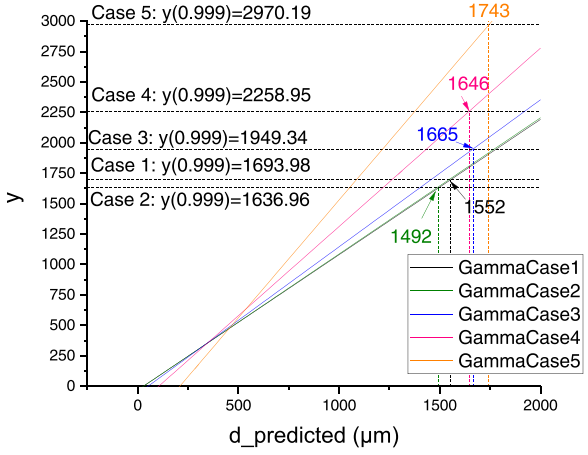

Fig. 13. Gamma regression lines for extrapolating maximum defect size, POT approach, cases 1–5.

Additionally, Figs. 12–13 show the plotted regression lines for the Weibull and Gamma CDFs with the best overall correlation coefficient values for the POT approach. The extrapolated maximum defect sizes are superimposed to better illustrate step 6 of the prediction procedure.

Conclusions

Geometrical defects are a common inhibitor of product performance in powder bed fusion (PBF) components. Understanding how to quantify the size and distribution of geometrical defects is key for certifying AM parts and improving printing processes. The

maximum defect size predicted to exist in the literature is dominantly based on the Gumbel CDF. In this study, a variety of geometric defects from an SS-316L block fabricated by selective laser melting was measured using the Feret caliper (FC) diameter. The measured data were then fitted to four different CDFs. The predictions from each CDF and the correlation coefficients (Pearson's R) were compared by both peak over the threshold (POT) and block maxima (BM) approaches of analyzing the porosity data. Six different data cases were tested based on the POT approach. The main results are as follows.

- The Weibull and Gamma CDFs showed similar predictions with a close agreement with the measured maxima of each POT data case.
- The Weibull and Gamma CDFs resulted in the highest R values for all POT cases.
- Sample size did not significantly affect correlation.
- All four CDFs correlated well to the porosity data for the POT approach, with all maximum R values being above 0.975.
- The Lognormal CDF had large prediction deviations with a zero-threshold data value and had consistently close predictions when the threshold value was increased.
- The BM approach predictions deviated from the measured maximum by large margins.
- Well-correlated regressions must also give realistic results to be useful.

Declaration of Competing Interest

The authors declare that they have no known competing financial interests or personal relationships that could have appeared to influence the work reported in this paper.

Acknowledgment

The authors would like to thank the financial support of the National Science Foundation under the grant CMMI-2152908.

References

[1] Masuo, H., Tanaka, Y., Morokoshi, S., Yagura, H., Uchida, T., Yamamoto, Y., Murakami, Y., 2018, Influence of Defects, Surface Roughness and HIP on the Fatigue Strength of Ti-6Al-4V Manufactured by Additive Manufacturing. International Journal of Fatigue, 117:163–179.
[2] Yu, C., Zhang, P., Zhang, Z., Liu, W., 2020, Microstructure and Fatigue Behavior of Laser-powder Bed Fusion Austenitic Stainless Steel. Journal of Materials Science and Technology, 46:191–200.
[3] Edwards, P., Ramulu, M., 2014, Fatigue Performance Evaluation of Selective Laser Melted Ti–6Al–4V. Materials Science and Engineering A, 598:327–337.
[4] Snow, Z., Nassar, A.R., Reutzel, E.W., 2020, Invited Review Article: Review of the Formation and Impact of Flaws in Powder Bed Fusion Additive Manufacturing. Additive Manufacturing, 36:101457.
[5] Gapinski, B., Wieczorowski, M., Marciniak-Podsadna, L., Pereira Domínguez, A., Cepova, L., Martinez Rey, A., 2018, Measurement of Surface Topography Using Computed Tomography. Springer International Publishing: 815–824.
[6] Mohr, G., Altenburg, S.J., Ulbricht, A., Heinrich, P., Baum, D., Maierhofer, C., Hilgenberg, K., 2020, In-Situ Defect Detection in Laser Powder Bed Fusion by Using Thermography and Optical Tomography—Comparison to Computed Tomography. Metals, 10/1: 103.
[7] Koutiri, I., Pessard, E., Peyre, P., Amlou, O., De Terris, T., 2018, Influence of SLM Process Parameters on the Surface Finish, Porosity Rate and Fatigue Behavior of As-built Inconel 625 Parts. Journal of Materials Processing Technology, 255:536–546.
[8] Deng, H., Liu, Q., Liu, H., Yu, H., 2018, Long-Life Fatigue of Carburized 12Cr2Ni Alloy Steel: Evaluation of Failure Characteristic and Prediction of Fatigue Strength. Metals, 8/12.
[9] Nadot, Y., Nadot-Martin, C., Kan, W.H., Boufadene, S., Foley, M., Cairney, J., Proust, G., Ridosz, L., 2020, Predicting the Fatigue Life of an AlSi10Mg Alloy Manufactured Via Laser Powder Bed Fusion by Using Data from Computed Tomography. Additive Manufacturing, 32:100899.
[10] Yukitaka Murakami, H.M., Tanaka, Yuzo, Nakatani, Masanori, 2019, Defect Analysis for Additively Manufactured Materials in Fatigue from the Viewpoint of Quality Control and Statistics of Extremes. Fatigue Design, 113–122.
[11] Mukherjee, T., DebRoy, T., 2018, Mitigation of Lack of Fusion Defects in Powder Bed Fusion Additive Manufacturing. Journal of Manufacturing Processes, 36:442–449.
[12] Gerdes, N., Hoff, C., Hermsdorf, J., Kaierle, S., Overmeyer, L., 2021, Hyperspectral Imaging for Prediction of Surface Roughness in Laser Powder Bed Fusion. International Journal of Advanced Manufacturing Technology, 115/4: 1249–1258.
[13] Sanaei, N., Fatemi, A., 2021, Defects in Additive Manufactured Metals and Their Effect on Fatigue Performance: A State-of-the-art Review. Progress in Materials Science, 117:100724.
[14] Shrestha, R., Simsiriwong, J., Shamsaei, N., 2021, Fatigue Behavior of Additive Manufactured 316l Stainless Steel Under Axial Versus Rotating-bending Loading: Synergistic Effects of Stress Gradient, Surface Roughness, and Volumetric Defects. International Journal of Fatigue, 144.
[15] Murakami, Y., Takagi, T., Wada, K., Matsunaga, H., 2021, Essential Structure of S-N curve: Prediction of Fatigue Life and Fatigue Limit of Defective Materials and Nature of Scatter. International Journal of Fatigue, 146.
[16] Murakami, Y., 1994, Inclusion Rating by Statistics of Extreme Values and Its Application to Fatigue Strength Prediction and Quality Control of Materials. Journal of Research of the National Institute of Standards and Technology, 99/4: 345–351.
[17] Alfieri, V., Argenio, P., Caiazzo, F., Sergi, V., 2016, Reduction of Surface Roughness by Means of Laser Processing over Additive Manufacturing Metal Parts. Materials (Basel), 10/1.
[18] Scherillo, F., 2019, Chemical Surface Finishing of AlSi10Mg Components Made by Additive Manufacturing. Manufacturing Letters, 19:5–9.
[19] Hatami, S., 2021, Variation of Fatigue Strength of Parts Manufactured by Laser Powder Bed Fusion. Powder Metallurgy, 1–6.
[20] Luo, Y.W., Zhang, B., Li, C.P., Chen, G.F., Zhang, G.P., 2019, Detecting Void-induced Scatter of Fatigue Life of Selective Laser Melting-fabricated Inconel 718 Using Miniature Specimens. Materials Research Express, 6/4:046549.
[21] Le, V.-D., Pessard, E., Morel, F., Prigent, S., 2020, Fatigue Behaviour of Additively Manufactured Ti-6Al-4V Alloy: The Role of Defects on Scatter and Statistical Size Effect. International Journal of Fatigue, 140:105811.
[22] Moran, T.P., Carrion, P.E., Lee, S., Shamsaei, N., Phan, N., Warner, D.H., 2022, Hot Isostatic Pressing for Fatigue Critical Additively Manufactured Ti-6Al-4V. Materials, 15/6: 2051.
[23] Yamashita, Y., Murakami, T., Mihara, R., Okada, M., Murakami, Y., 2018, Defect Analysis and Fatigue Design Basis for Ni-based Superalloy 718 Manufactured by Selective Laser Melting. International Journal of Fatigue, 117:485–495.
[24] Mower, T.M., Long, M.J., 2016, Mechanical Behavior of Additive Manufactured, Powder-bed Laser-fused Materials. Materials Science and Engineering, A, 651:198–213.
[25] Boyce, B.L., Salzbrenner, B.C., Rodelas, J.M., Swiler, L.P., Madison, J.D., Jared, B.H., Shen, Y.-L., 2017, Extreme-Value Statistics Reveal Rare Failure-Critical Defects in Additive Manufacturing. Advanced Engineering, 19/8:1700102.
[26] Wu, Z., Wu, S., Bao, J., Qian, W., Karabal, S., Sun, W., Withers, P.J., 2021, The Effect of Defect Population on the Anisotropic Fatigue Resistance of AlSi10Mg Alloy Fabricated by Laser Powder Bed Fusion. International Journal of Fatigue, 151:106317.
[27] Sombatmai, A., Uthaisangsuk, V., Wongwises, S., Promoppatum, P., 2021, Multiscale Investigation of the Influence of Geometrical Imperfections, Porosity, and Size-dependent Features on Mechanical Behavior of Additively Manufactured Ti-6Al-4V Lattice Struts. Materials and Design, 209:109985.
[28] Hu, Y.N., Wu, S.C., Wu, Z.K., Zhong, X.L., Ahmed, S., Karabal, S., Xiao, X.H., Zhang, H.O., Withers, P.J., 2020, A New Approach to Correlate the Defect Population with the Fatigue Life of Selective Laser Melted Ti-6Al-4V Alloy. International Journal of Fatigue, 136:105584.
[29] Gordon, J.V., Narra, S.P., Cunningham, R.W., Liu, H., Chen, H., Suter, R.M., Beuth, J.L., Rollett, A.D., 2020, Defect Structure Process Maps for Laser Powder Bed Fusion Additive Manufacturing. Additive Manufacturing, 36:101552.
[30] Zhang, M., Sun, C.-N., Zhang, X., Goh, P.C., Wei, J., Hardacre, D., Li, H., 2017, Fatigue and Fracture Behaviour of Laser Powder Bed Fusion Stainless Steel 316L: Influence of Processing Parameters. Materials Science and Engineering, A, 703:251–261.
[31] Oberreiter, M., Fladischer, S., Stoschka, M., Leitner, M., Probabilistic, A., 2022, Fatigue Strength Assessment in AlSi-Cast Material by a Layer-Based Approach. Metals, 12/5: 784.
[32] Romano, S., Brandão, A., Gumpinger, J., Gschweitl, M., Beretta, S., 2017, Qualification of AM Parts: Extreme Value Statistics Applied to Tomographic Measurements. Materials and Design, 131:32–48.
[33] Juan, R., Wang, M., Lian, J., Gu, C., Li, L., Bao, Y., 2021, Quantifying the Comprehensive Characteristics of Inclusion-Induced Defects Using an Integrated Destructive and Non-Destructive Method. Materials, 14/6: 1475.
[34] Hastie, J.C., Kartal, M.E., Carter, L.N., Attallah, M.M., Mulvihill, D.M., 2020, Classifying Shape of Internal Pores Within AlSi10Mg Alloy Manufactured by Laser Powder Bed Fusion Using 3D X-ray Micro Computed Tomography: Influence of Processing Parameters and Heat Treatment. Materials Characterization, 163:110225.
[35] Murakami, Y., Endo, M., 1986, Effects of Hardness and Crack Geometries on ΔKth of Small Cracks Emanating from Small Defects. Miller KJ, de Los Rios ER, (Eds.) The Behavior of Short Fatigue Cracks, EGF Pub. 1. Mechanical Engineering Publications, London: 275–293.
[36] Yukitaka, M., Masahiro, E., 1983, Quantitative Evaluation of Fatigue Strength of Metals Containing Various Small Defects or Cracks. Engineering Fracture Mechanics, 17/1: 1–15.

[37] Anderson, C.W., Shi, G., Atkinson, H.V., Sellars, C.M., Yates, J.R., 2003, Interrelationship between Statistical Methods for Estimating the Size of the Maximum Inclusion in Clean Steels. Acta Materialia, 51/8: 2331–2343.
[38] Murakami, Y., Endo, T., 1980, Effects of Small Defects on Fatigue Strength of Metals. International Journal of Fatigue, 2/1: 23–30.
[39] Wang, Q.G., Jones, P.E., 2007, Prediction of Fatigue Performance in Aluminum Shape Castings Containing Defects. Metallurgical and Materials Transactions B, 38/4: 615–621.
[40] Nicoletto, G., Konečná, R., Fintova, S., 2012, Characterization of Microshrinkage Casting Defects of Al-Si Alloys by X-ray Computed Tomography and Metallography. International Journal of Fatigue, 41:39–46.
[41] Gumbel, E.J., 1957, Statistics of Extremes. Columbia University Press, New York, NY, USA. pp. 1–36, 82, 113, 156–159.
[42] Holický, M., 2013, Selected Models of Continuous Variables. Springer, Berlin Heidelberg: 63–78.